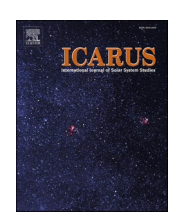


Contents lists available at ScienceDirect

# Icarus

journal homepage: www.elsevier.com/locate/icarus





# Space weathering on Vesta: Ion bombardment induced changes on HEDs in visible and infrared reflectance

Stefano Rubino <sup>a,b,\*</sup>, Francesca Zambon <sup>a</sup>, Rosario Brunetto <sup>b</sup>, Océane Barraud <sup>c</sup>, Sébastien Besse <sup>d</sup>, Ferenc Borondics <sup>e</sup>, Cristian Carli <sup>a</sup>, Jean-Philippe Combe <sup>f</sup>, Kerri Donaldson-Hanna <sup>g</sup>, Rachel Klima <sup>h</sup>, Cateline Lantz <sup>b</sup>, Giovanni Pratesi <sup>i</sup>, Katrin Stephan <sup>c</sup>, Federico Tosi <sup>a</sup>

- <sup>a</sup> INAF Istituto di Astrofisica e Planetologia Spaziali, Rome, Italy
- <sup>b</sup> Institut d'Astrophysique Spatiale, Université Paris-Saclay, Orsay, France
- Institute of Planetary Research (DLR), Berlin, Germany
- <sup>d</sup> Aurora Technology B.V. for ESA, Madrid, Spain
- e SMIS beamline, SOLEIL Synchrotron, Gif-sur-Yvette, CEDEX, France
- f Planetary Science Institute, Tucson, AZ, USA
- g University of Central Florida, Physical Sciences Building (PSB), Orlando, FL, USA
- <sup>h</sup> Johns Hopkins University Applied Physics Laboratory, USA
- <sup>1</sup> Università degli studi di Firenze, Dipartimento di Scienze della Terra, Florence, Italy

#### ARTICLE INFO

#### Keywords: Vesta Space weathering Ion bombardment Spectroscopy

#### ABSTRACT

The NASA/Dawn mission targeted *V*-type asteroid (4) Vesta between 2011 and 2012. The mission confirmed Vesta as the parent body of most of the HED meteorite family and led an extensive mapping of the surface's spectral properties. The well-pronounced different spectroscopic features of Vesta suggest that this body has its own form of space weathering. In this work, we look for the optimal parameter space for distinguishing between fresh and weathered materials on Vesta and other V-type objects. We emulated the effects of the solar wind component of space weathering by performing ion bombardment experiments with 40 keV He<sup>+</sup> on four HED meteorites. We then studied the spectral behavior of our artificially weathered samples, spanning from the visible to the mid-infrared range, using several spectral parameters. We observed that in the visible and near-IR range, the evolution of eight parameters – darkening of reflectance at 380–465-550 nm, decrease in band depth and band area of the 1-µm absorption feature, and reddening of three different spectral slopes - are enough to distinguish between differences in mineral composition and weathering state among our samples. In the mid-IR, we detected a consistent red shift in the position of the Reststrahlen feature, associated with sample weathering. These findings can provide support for the interpretation of remote sensing data from *V*-type objects, aiding in the assessment of mineralogical differences and the weathering state of surface materials.

# 1. Introduction

V-type asteroid (4) Vesta is one of the largest basaltic bodies in the main asteroid belt, with an Fe-rich core, a silicate mantle, and a basaltic crust (McCord et al., 1970; Mittlefehldt, 2015), possibly not completely differentiated (Park et al., 2025). After being studied by ground-based telescopes and the Hubble Space Telescope (McCord et al., 1970; Binzel et al., 1997; Li et al., 2011), between 2011 and 2012, Vesta was extensively mapped and observed by the NASA Dawn mission (Russell

and Raymond, 2012). The international community gained a new perspective on differentiated asteroidal bodies, and the data acquired during this scientific endeavor remains of interest today. Dawn confirmed Vesta as the parental body of the differentiated meteorite families, howardites, eucrites, and diogenites (HEDs) related to Vesta's regolith, basaltic crust, and olivine-rich mantle - bearing out the link with V-type asteroids (McCord et al., 1970; Hiroi et al., 1994; Ammannito et al., 2013; De Sanctis et al., 2013; McSween Jr et al., 2013). It is worth noting that some HEDs exhibit distinct oxygen isotopic

<sup>\*</sup> Corresponding author: Stefano Rubino, INAF - Istituto di Astrofisica e Planetologia Spaziali, Rome, Italy. E-mail address: stefano.rubino@inaf.it (S. Rubino).

compositions, suggesting that their parent body may be a V-type object other than Vesta (Scott et al., 2009; Mittlefehldt et al., 2022). Additionally, compositional surface maps highlighted the presence of hydrated exogenous materials on Vesta's surface, originating from outer space impactors (Reddy et al., 2012; De Sanctis et al., 2012; McCord et al., 2012; Combe et al., 2015). Finally, Pieters et al. (2012) investigated the effects of space weathering (SpWe) on Vesta - a topic more closely related to the scope of this work. SpWe on Vesta still represents a significant conundrum due to Vesta's spectroscopic properties in the near-IR compared to lunar-type space weathered features (e.g., reddening - increase of spectral slope for longer wavelengths, darkening, weakening of absorption features; Denevi et al., 2024 and references therein). The well-pronounced (pyroxene) absorption bands suggest the absence of lunar-like nanophase iron on Vesta as a product of SpWe (observed on the Moon - Noble et al., 2010a, b - and Itokawa samples -Noguchi et al., 2014. Slope failures due to impact processes on Vesta's steep slopes highly contribute to regolith resurfacing processes (Krohn et al., 2014a, 2014b; Jaumann et al., 2012), which complexify Vesta's geological history and, in turn, contribute to diluting the spectral effects of classical SpWe tracers - such as slope reddening and darkening - on older, more weathered materials. Moreover, the protection from a remanent magnetic field could also avoid direct exposure of Vesta's surface to solar wind weathering (Vernazza et al., 2006; Fu et al., 2012). Hence, to better identify the weathering state of surfaces on V-type asteroids, SpWe effects must be investigated on this type of material while expanding the parameter space used.

To perform these investigations, we can emulate the effects of SpWe on Vesta in a laboratory environment by using HEDs as analogue material for Vesta's surface and processing these materials to reproduce the conditions of SpWe. There are a limited number of experimental studies focusing on such a topic. Pulsed laser irradiation experiments on HEDs emulating the effects of the micrometeorite component of SpWe identified various spectral effects, including darkening and reddening in the visible/near-IR, coupled with the weakening of the absorption bands at 1 and 2 µm, typical of pyroxenes in HEDs (Hiroi and Pieters, 1998; Hiroi et al., 2013). Ion bombardment experiments, which focus on replicating the solar wind component of SpWe, have shown similar effects, highlighting that different HEDs exhibit different levels of reddening for the same weathering stage (Vernazza et al., 2006; Fulvio et al., 2012). Due to experimental constraints, previous works have often used heavy ions such as C<sup>+</sup>, Ar<sup>+</sup>, and Ar<sup>2+</sup> at energies higher than those related to their ion population in the solar wind. Moreover, most works only have measured samples ex-situ after irradiation, focusing on the visible to near-IR spectral range. To provide further insight regarding the effects of the solar wind component of SpWe on V-type asteroids, we present a new study based on an ion implantation experiment. We used He<sup>+</sup> ions, the second most abundant ion population in the solar wind, by following in situ the spectral changes upon weathering in the visible and near-infrared ranges and expanding the overall spectral dataset range by examining spectral changes in the mid-infrared. More specifically, the following work consists of performing He<sup>+</sup> ion implantation on pellets made out of four HEDs, i.e. three eucrites (E) and one diogenite-olivine (D), to emulate the effects of SpWe on V-type surfaces. Upon weathering, we monitored the in-situ spectral evolution of our samples in the visible and near-IR range to investigate which parameters are more sensitive to ion implantation and provide support for future remote sensing analysis of V-type objects. Further data was acquired ex-situ in the mid-IR range to probe the evolution of the silicate stretching features around 10 μm.

#### 2. Materials and methods

# 2.1. The samples

We performed ion implantation experiments on four HED meteorites from North West Africa: NWA 4968 (E), NWA 6909 (E), NWA 7234 (E), and NWA 6232 (D). These meteorites were chosen since their

mineralogy, bulk composition and petrography had already been well characterized via optical investigation, scanning electron microscopy (SEM), energy-dispersive X-ray spectroscopy (EDS) and microprobe analysis (EPMA) (Carli et al., 2018, 2022), allowing us to probe the link between mineralogy and ion bombardment effects. In this work, we use the same samples described in Carli et al. (2018, 2022). The main mineralogy and petrography are summed up here:

- NWA 4968: major phases are pyroxenes (mainly pigeonite with augitic exsolution lamellae) and plagioclase (anorthite); minor phases are ilmenite, chromite and silica polymorphs. It is a polymict breccia which consists of fine to medium-grained ophitic to subophitic basalts and low weathering grade.
- NWA 7234: major phases are pyroxenes (mainly pigeonite with augitic exsolution lamellae), plagioclase (anorthite); minor phases are ilmenite, chromite and silica polymorphs. It is a polymict breccia composed of exsolved pyroxenes and calcic plagioclase fragments as well as lithic clasts including basaltic lithologies and shock-melt veins and a medium weathering grade.
- NWA 6909: major phases are pyroxenes (predominantly low-calcium pyroxenes LCP), plagioclase (anorthite); minor phases are ilmenite, chromite, silica polymorph and troilite. It features a subophitic texture with calcic plagioclase grains (blocky to lath-shaped) that are partly enclosed within strongly zoned pigeonite and exhibits a low weathering grade.
- NWA 6232 major phases are olivine, pyroxenes (predominantly LCP); minor phases are chromite and troilite. It exhibits a heterogeneous overall texture characterized by zones dominated by olivine (tens of µm to mm) and orthopyroxene.

Note that NWA 4968 and NWA 7234 appear very similar mineralogically. However, NWA 4968 is characterized by finer-grained clasts with respect to NWA 7234, which is a breccia-type rock, incorporating different lithologies (basaltic and shocked-melt).

The oxide composition of mafic phases (Table 1) was used to derive ion implantation parameters via the SRIM - Stopping and Range of Ions in Matter code (Ziegler et al., 2010).

The sample preparation method has already been employed in previous ion implantation experiments focusing on carbonaceous chondrites (Brunetto et al., 2014; Lantz et al., 2015, 2017) and terrestrial phyllosilicates (Rubino et al., 2020; Rubino et al., 2024). For each meteorite stone, we produced one 13-mm diameter pellet by pressing approximately 130 mg of meteorite powder onto a PEG substrate (powdered polyethylene glycol with an average molecular mass of 8000 g/mol, from Fisher Scientific) for 5 min, under a weight of 7 tons (see Fig. 1). The produced meteorite layer is thick enough (>500  $\mu$ m) to

Table 1
Mineral chemistry for the main phases of our samples, derived by electron probe microanalysis (EPMA) for NWA 4968, NWA 7234, NWA 6909 and NWA 6232. Data is in wt%. Adapted from Carli et al., 2018–2022. (E: eucrite, D: diogenite, LCP: low-calcium pyroxene, HCP: high-calcium pyroxene, Ol: olivine, bd: below the detection limit).

|                                | NWA 4968 (E) |                 | NWA 7234 (E)    |                 | NWA 6909<br>(E) | NWA 6232<br>(D) |      |
|--------------------------------|--------------|-----------------|-----------------|-----------------|-----------------|-----------------|------|
|                                | LCP          | HCP             | LCP             | HCP             | LCP             | LCP             | Ol   |
| SiO2                           | 49.10        | 50.42           | 48.88           | 55.42           | 49.57           | 54.7            | 37.4 |
| TiO₂                           | 0.23         | 0.42            | 0.16            | 0.38            | 0.34            | 0.1             | 0.0  |
| Al₂O₃                          | 0.22         | 0.68            | 0.15            | 0.51            | 0.74            | 0.4             | 0.0  |
| Cr <sub>2</sub> O <sub>3</sub> | 0.08         | 0.24            | 0.04            | 0.19            | 0.35            | 0.5             | 0.1  |
| FeO                            | 35.95        | 18.72           | 38.13           | 17.70           | 29.57           | 15.7            | 26.2 |
| MnO                            | 1.03         | 0.57            | 1.10            | 0.54            | 0.87            | 0.5             | 0.6  |
| MgO                            | 11.47        | 10.07           | 11.48           | 9.97            | 13.09           | 27.1            | 35.8 |
| CaO                            | 2.52         | 19.18           | 1.05            | 20.83           | 5.85            | 1.0             | 0.1  |
| Na <sub>2</sub> O              | 0.08         | 0.11            | 0.04            | 0.11            | 0.05            | 0.0             | 0.0  |
| K <sub>2</sub> O               | 0.04         | 0.02 (b.<br>d.) | 0.01 (b.<br>d.) | 0.01 (b.<br>d.) | 0.03 (b.d.)     | 0.0             | 0.0  |

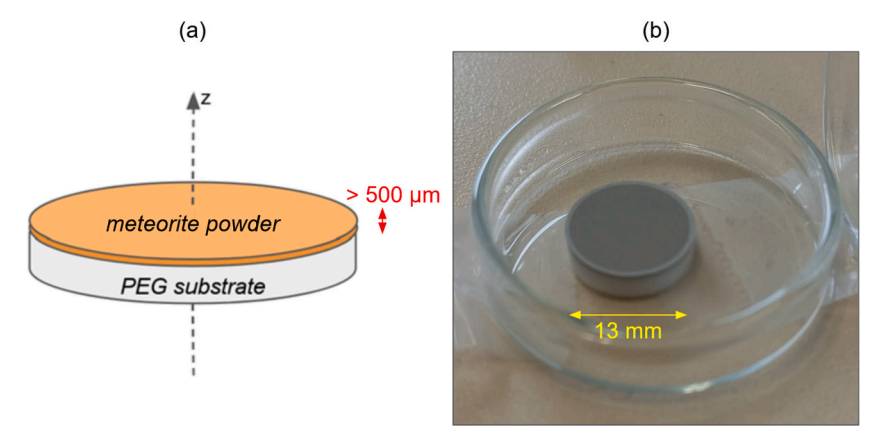


Fig. 1. (a) Schematic of a pressed powder meteorite pellet. (b) Pressed powder pellet of NWA 7234 after ion bombardment. The brighter rim is pristine material that the sample holder masked during the ion bombardment process.

prevent He $^+$  ions (see the SRIM results in section II.2) or photons (typically probing layers from a few  $\mu m$  to hundreds of  $\mu m$  thick in the visible to mid-IR range - see discussion in Brunetto et al., 2020) from interacting with the PEG layer. An agate mortar and pestle were used to obtain the meteorite powder, coupled with a sieving column to separate different grain sizes. The pellets NWA 6232 and NWA 7234 were made from powder with a grain size smaller than 50  $\mu m$ , while pellets for NWA 6909 and NWA 4968 were made from powder with a grain size smaller than 75  $\mu m$ . The difference is due to a lack of material to produce the pellets for NWA 6909 and NWA 4968. Both grain sizes remain coherent, with Vesta's mineral phases being all, on average, smaller than 100  $\mu m$  except olivine (Poulet et al., 2015).

# 2.2. In-situ characterization: the INGMAR-SIDONIE platform, ion implantation conditions, and visible to near-IR data acquisition

We performed the ion implantation experiments in the INGMAR (IrradiatioN de Glaces et Météorites Analysées par Réflectance, Institut d'Astrophysique Spatiale (IAS) - Laboratoire des deux Infinis Irène Joliot Curie (IJCLab, Orsay) vacuum chamber. The implantation was done at room temperature under a vacuum ( $\sim 10^{-7}$  mbar). The vacuum chamber is connected to the SIDONIE ion implanter (Chauvin et al., 2004 -IJCLab, Orsay), which provided the He<sup>+</sup> beam at 40 keV with a relatively low flux of  $\sim 10^{13}$  ions cm<sup>-2</sup> s<sup>-1</sup>. Subsequent use of the ion implanter allowed us to weather and monitor the evolution of the pellets at different fluences:  $1 \times 10^{16}$ ,  $3 \times 10^{16}$ , and  $6 \times 10^{16}$  ions/cm<sup>2</sup>. The SRIM code enabled us to estimate the ion implantation depth and energy transfer in our experiment (see Table 2). There are two different regimes for energy transfer: inelastic collision, which is related to the energy loss of electrons, and elastic collision, which is related to the energy loss of nuclei. These parameters were derived by inputting into the SRIM code a density of 2.9 g/cm<sup>3</sup> for high-Ca pyroxene (HCP), 4.0 g/cm<sup>3</sup> for low-Ca

**Table 2** SRIM results simulation for 40 keV He<sup>+</sup> implantation in our samples.

| Meteorite | Phase   | Stopping Power<br>[keV/µm] | Implantation depth |      |  |
|-----------|---------|----------------------------|--------------------|------|--|
|           |         | dE/dx<br>inelastic         | dE/dx<br>elastic   | [nm] |  |
|           | LCP     | $1.83 \times 10^{2}$       | 8.19               | 220  |  |
| NWA 4968  | HCP     | $1.35\times10^2$           | 6.12               | 300  |  |
|           | LCP     | $1.82 \times 10^2$         | 8.15               | 220  |  |
| NWA 7234  | HCP     | $1.36\times10^2$           | 6.16               | 300  |  |
| NWA 6909  | LCP     | $1.86 \times 10^2$         | 8.31               | 217  |  |
|           | LCP     | $2.02 \times 10^2$         | 8.74               | 206  |  |
| NWA 6232  | Olivine | $2.16\times10^2$           | 9.32               | 190  |  |

pyroxene, and 4.4 g/cm<sup>3</sup> for olivine, which correspond respectively to the theoretical density values for wollastonite, ferrosilite, and fayalite.

Regardless of their mineral phase, the inelastic collision regime dominates all samples over the elastic one for 40 keV He<sup>+</sup>, so we expect ion implantation effects due to ionization of the surface rather than the creation of vacancies or replacement (associated with elastic collisions, see Brunetto and Strazzulla, 2005). The ion penetration depths vary approximately from 200 to 300 nm. This length is far smaller than the photon probing depth for pyroxenes in the visible range (a few hundred  $\mu m$ ; photon probing depth is related to k, the imaginary part of the refractive index, which for pyroxenes ranges approximately from  $10^{-5}$  to  $10^{-3}$  (Denevi et al., 2007), with maxima associated with the 1- $\mu m$  and 2- $\mu m$  features). The collected reflectance spectra in the visible and near-IR will thus have contributions from the ion bombarded surface layer and the pristine sub-surface.

The ion beam bombarded the whole surface of each pellet, except a small external corona ( $\sim$ 500  $\mu$ m in width), which was masked by the sample holder (see Fig. 2). After bombardment, the samples were removed from the INGMAR mounting racket by using tweezers and lattice gloves. The samples were then put in plastic containers and kept in a desiccator. During this removal procedure, the surface of the NWA 4968 and NWA 6909 pellets was damaged due to decohesion between the meteorite layer and the PEG substrate, and thus the ion bombarded surface was lost.

Optic fibers interfaced with the INGMAR vacuum chamber allowed us to acquire in-situ reflectance spectra in the visible and near-IR range (from 0.35 to 4  $\mu m$ ) of the pellets' surface in their pristine state and at the various implantation steps to monitor their spectral evolution with the increase of the ion fluence. The observation geometry of the spectroscopic setup is fixed. Illumination angles for the visible and near-IR light sources are  $i = 15^{\circ}$  and  $20^{\circ}$ , respectively, from the normal to the pellets' surfaces, but on different planes to avoid specular reflection. The illumination spot sizes are 20 mm and 12 mm in diameter for the visible and near-IR sources, respectively. The reflected signal is collected using a single optical fiber with a 3-4 mm diameter collection spot and a fixed collection angle  $e=15^{\circ}$ . The phase angle is  $20^{\circ}$  for visible and  $15^{\circ}$  for near-IR, with regard to the 3D geometry of the setup. The angles are fixed due to the setup's conception, hence why these measurements are not carried out in the standard viewing geometry of a 30° phase angle. It is relevant to address that, for bidirectional reflectance measurements such as the one carried out here, there are specific geometric configurations that maximize the contribution from the utmost top layers of our samples (Rubino et al., 2022), such as working at near-Nadir configuration - meaning observing close the surface's normal - with a small

Spectral data from 0.35 to  $1.1~\mu m$  are acquired using a Maya2000Pro grating spectrometer (Ocean Optics) at a spectral resolution of 0.5~nm,

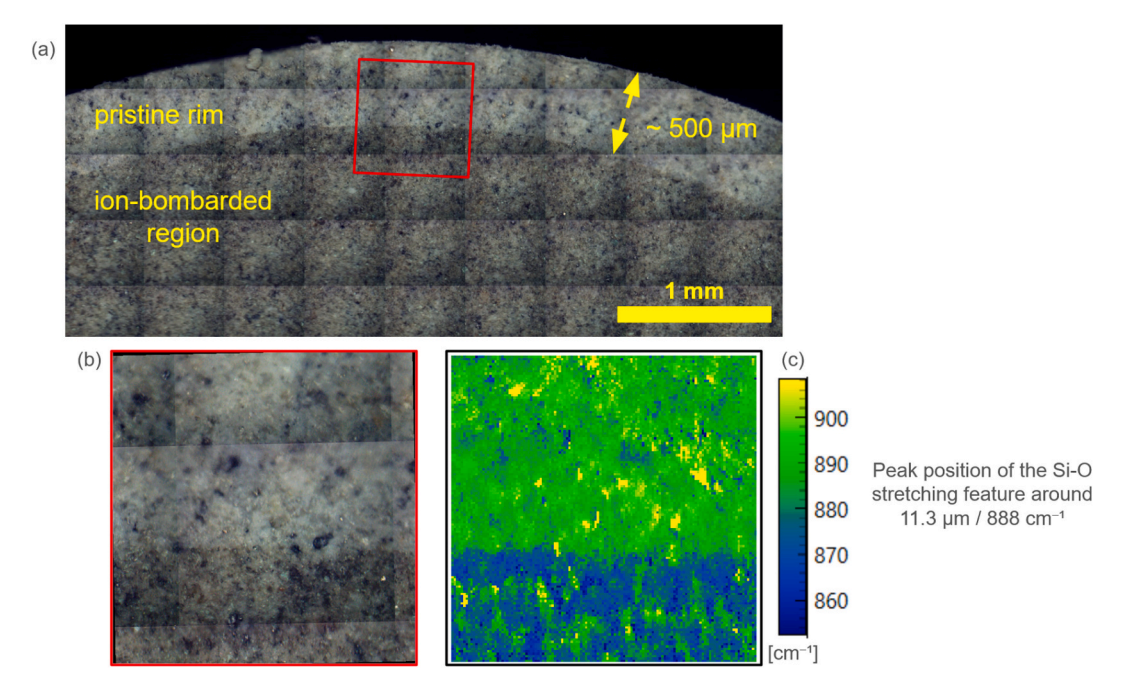


Fig. 2. (a) Top view of the ion bombarded NWA 7234 pellet, focusing on the pellet's rim. (b) Zoomed-in view of a region of interest on the pellet's rim. (c) Map of the peak position variations associated with the Si—O stretching feature near 11.3  $\mu$ m / 888 cm in the pyroxene-dominated matrix of NWA 7234, extracted from the reflectance spectra.

with 200 scans (each with an exposure time of 200 ms). A Tensor 37 FTIR spectrometer (Bruker) collects data beyond 1  $\mu m$ , with a spectral resolution of  $16~cm^{-1}$  (corresponding to 1.6~nm around 1  $\mu m$  and 26~nm at the upper limit of 4  $\mu m$ ). A scaling factor is applied to the vis/near-IR (0.35–1.1  $\mu m$ ) spectrum to scale it with respect to the near-IR (1–4  $\mu m$ ) spectrum. The scaling factor is obtained by computing the ratio between the barycenters of the spectral data over the overlapping range (1–1.1  $\mu m$ ), fluence by fluence. Spectra acquired with the INGMAR setup are reproducible (the collection spot for each sample is always the same, with an error of less than 100  $\mu m$ ; Lantz et al., 2017). The estimated error in the reflectance is approximately 1 %, attributed to fluctuations in the light sources.

# 2.3. Ex-situ characterization: mid-IR data acquisition

An FTIR micro-spectrometer (Agilent Cary 670/620) with an internal source located at the SMIS beamline of the SOLEIL synchrotron (France) allowed us to perform the mid-IR characterization of our pellets. These measurements were acquired ex situ (at atmospheric temperature and pressure) directly on the ion bombarded pellets. We acquired spectra from

2.5 to 12  $\mu$ m with respect to a gold reference, using a 15× objective with a numerical aperture of 0.62, with 256 scans at a spectral resolution of 4  $cm^{-1}$  (corresponding to a resolution of 2.5 nm at 2.5  $\mu m$  and 56 nm at 12  $\mu$ m). We managed to acquire mid-IR data only for the NWA 7234 and NWA 6232 pellets, as the surface of the other two pellets was damaged upon extraction from the vacuum chamber. We acquired hyperspectral maps (704  $\times$  704  $\mu m,$  spatial resolution of 5.5  $\mu m)$  using a Focal Plane Array (FPA) detector. We acquired data from the center of the pellets and over the non-bombarded rim to investigate both weathered and unweathered material from the same pellet. Due to the experimental schedule, the center of the pellets could not be characterized before the weathering experiment. We are thus comparing spectral data from two different regions of our pellets, which may complicate the interpretation of the data. However, the hyperspectral maps allowed us to estimate that these pressed-powder pellets are mineralogically homogeneous enough for such a comparison at the scale of the maps (the Regions Of Interest (ROIs) size are larger than 200 μm),

the reflectance differences being due to different crystal orientation, not mineral distribution (see Appendix A).

#### 2.4. Spectral analysis and parameter derivation

The spectral analysis of the considered dataset has been done via Python scripts, IDL scripts, the ENVI geospatial analysis, the QGIS software and the Quasar spectroscopic add-on (Toplak et al., 2021) of the Orange dataframe suite. Several spectral parameters, more thoroughly presented in the following section, were considered for this study. Band centers are assimilated to band minima and derived after removing a linear continuum. The linear continuum anchor points are defined as the local left and right maxima adjacent to the spectroscopic band (see Clark and Roush, 1984). Spectral slopes between i and j given in µm are computed following the definition of Filacchione et al. (2012) and Cuzzi et al. (2009), by the best fitting linear trend to the reflectance R in the spectral range between i and j:

$$S_{ij} = rac{R_j - R_i}{R_i imes (j-i)}$$

In the mid-IR range, the spectral analysis is focused on the position of the Christiansen feature (C·F.) – a reflectance minimum occurring near the wavelength where the material's refractive index equals that of the surrounding medium - and the Reststrahlen bands (R.B) - associated with fundamental vibrational modes on a mineral crystal lattice -, both indicators of a sample's mineralogy and weathering degree (see Brunetto et al., 2020). A linear continuum drawn using the C.F. as the sole anchor point has been subtracted from the mid-IR data prior to spectral parameter derivation.

#### 3. Results

# 3.1. Visible to near-IR data and parameter space

In Fig. 3, we show the spectral evolution of the NWA 4968 pellet upon 40 keV He<sup>+</sup> ion implantation. The complete visible to near-IR spectral dataset, including data from the other pellets, is shown in

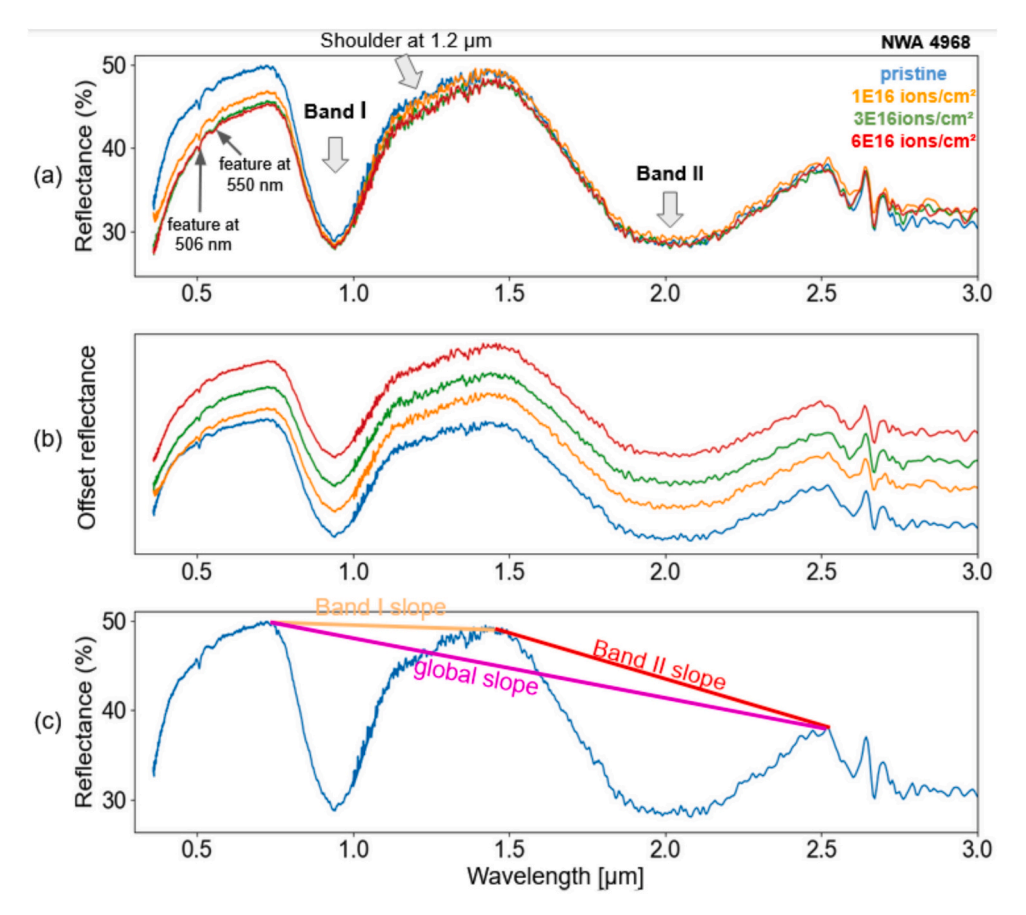


Fig. 3. Spectral dataset of the NWA 4986 pellet, wavelength vs. reflectance. (a) Evolution of NWA 4968 upon 40 keV He $^+$  ion implantation. Key spectroscopic features are highlighted. Fluences from top to bottom near 700 nm: 0 ions/cm $^2$  (pristine),  $1 \times 10^{16}$  ions/cm $^2$ ,  $3 \times 10^{16}$  ions/cm $^2$ ,  $6 \times 10^{16}$  ions/cm $^2$ . (b) Offset reflectance of the NWA 4968 dataset. Fluences from bottom to top: 0 ions/cm $^2$  (pristine),  $1 \times 10^{16}$  ions/cm $^2$ ,  $3 \times 10^{16}$  ions/cm $^2$ ,  $6 \times 10^{16}$  ions/cm $^2$ . (c) The pristine spectrum of NWA 4968, showcasing some of the spectral slopes investigated in this work.

Appendix B. Some key spectroscopic features are highlighted, such as:

- The broad features at 1  $\mu$ m and 2  $\mu$ m Band I and Band II, typical of the pyroxene component in HEDs, associated with spin-allowed crystal field transitions in Fe<sup>2+</sup> occupying the M2 crystallographic site (Cloutis and Gaffey, 1991 and references therein);
- A broad shoulder at approximately 1.1–1.2 μm, associated with Fe<sup>2+</sup> occupying the M1 crystallographic site (Klima et al., 2007). For very high concentrations of plagioclase, the 1.1 to 1.3 μm feature of plagioclase may also contribute to this signal (Donaldson et al., 2012; Ohtake et al., 2009);
- Two weak spectroscopic absorption features at 506 and 550 nm, associated with spin-forbidden crystal field transitions in Fe<sup>2+</sup> located in the M2 site of pyroxene (Cloutis et al., 2010 and references therein).

We observe a general reddening of the spectral slopes and changes in Band I and Band II areas associated with weathering, such as band depth decrease. To better investigate and quantify the effects of He<sup>+</sup> ion implantation on our HED sample, we define a parameter space that is independent of ion fluence. This parameter space aims to maximize the data spread to distinguish spectral variations due to composition from those caused by weathering. Machine learning algorithms or clustering methods such as Principal Component Analysis (PCA) may yield similar results. However, the goal here is to play with parameters already frequently used and known by the remote sensing community, which may be faster/easier to apply than machine-learning algorithms and have direct "physical" meaning and implication. We start with an initial parameter space comprising 25 spectral parameters (see Table 3 for the

definition of each parameter as well as Appendix C for the evolution of each parameter as a function of ion fluence). The work presented here is part of a broader project (ISSI International Team project n° 485 - Deciphering Compositional Processes in Inner Airless Bodies of our Solar System; Zambon et al., 2022) which focuses also on other basaltic airless bodies such as the Moon, hence why the Clementine ratio data (Speyerer et al., 2023) have been considered here.

To reduce the number of parameters and retain only those exhibiting the most noticeable changes upon weathering, we introduce the following criteria:

- The retained spectral parameter must exhibit a common trend identifiable across all four weathered samples.
- The smallest relative variation across our samples between the initial value of the retained parameter and its value at the end of the ion implantation experiment must be significant. This variability is computed as such (1):

$$variability_{i} = Minimum \frac{P_{max\ fluence}^{i} - P_{pristine}^{i}}{P_{pristine}^{i}}$$
 (1)

with p as the investigated parameter and i as the associated sample.

After quickly scanning through the evolution of individual parameters as a function of He<sup>+</sup> ion fluence (see Appendix B), we selected the following parameters according to the two criteria described above:

- Reflectance at 380, 465, and 550 nm;
- Band I depth and area;
- $\bullet\,$  Band I and Band II spectral slopes and the global slope.

**Table 3**All parameters selected for this investigation, their acronym and their variability (%) as defined in formula (1). \*The limits for the Band I and Band II spectral slopes change depending on the shoulder/band position, as stated in II.4.

| Parameter                           | Definition   | variability<br>(%) |
|-------------------------------------|--|--------------------|
| R <sub>380</sub>                    | Reflectance at 380 nm  | 18.53              |
| R <sub>465</sub>                    | Reflectance at 465 nm  | 13.64              |
| R <sub>550</sub>                    | Reflectance at 550 nm  | 10.75              |
| R <sub>730</sub>                    | Reflectance at 730 nm  | 9.88               |
| BC1                                 | Band I center  | 0                  |
| BD1                                 | Band I depth   | 6.46               |
| BA1                                 | Band I area  | 6.37               |
| C1                                  | Band I centroid  | 0.29               |
| BC2                                 | Band II center   | 0.15               |
| BD2                                 | Band II depth  | 1.89               |
| BA2                                 | Band II area   | 1.9                |
| C2                                  | Band II centroid   | 0.97               |
| BAR                                 | Band area ratio between Band I and Band II   | 3.06               |
| BD <sub>506</sub>                   | Band depth at 506 nm   | 7.8                |
| Slope<br>380-465                    | Spectral slope between 380 and 465 nm  | 8.85               |
| Slope<br>465–730                    | Spectral slope between 465 and 730 nm  | 1.84               |
| Slope I                             | *Spectral slope between the shoulders of Band I                                      | 340                |
| Slope II                            | *Spectral slope between the shoulders of Band II                                     | 2.38               |
| Slope G                             | Global slope - between the left shoulder of Band I and the right shoulder of Band II | 31.58              |
| $R_{730}/R_{550}$                   | Reflectance ratio  | 1.53               |
| $R_{465}/R_{550}$                   | Reflectance ratio  | 3.29               |
| $R_{380}/R_{550}$                   | Reflectance ratio  | 6.46               |
| $R_{730}/R_{415}$                   | Reflectance ratio as for lunar Clementine data (                                     | 9.47               |
|                                     | Speyerer et al., 2023)   |                    |
| R <sub>730</sub> /R <sub>1000</sub> | Reflectance ratio as for lunar Clementine data                                       | 5.6                |
| R <sub>415</sub> /R <sub>730</sub>  | Reflectance ratio as for lunar Clementine data                                       | 8.71               |

This reduced selection prompted us to define three parameter subspaces to investigate the effects of ion implantation on our weathered HEDs: the reflectance space (R380 - R465  $\cdot$  R550), the Band I space (BD1, BA1), and the slope space (Slope G—Slope I—Slope II). In Fig. 4, these three parameter subspaces help us visualise spectral changes in our entire VIS-NIR dataset.

All samples exhibit various darkening instances in the reflectance space upon reaching the maximum ion fluence, from  $-7.6\,\%$  for R550 in NWA 6909 to  $-29.8\,\%$  for R380 in NWA 7234 (Fig. 4 panel a). Data associated with our samples' pristine state appear aligned, while data

associated with the higher fluences -  $1 \times 10^{16}$ ,  $3 \times 10^{16}$  and  $6 \times 10^{16}$ ions/cm<sup>2</sup> - diverge from this alignment. The band area for Band I continually decreases as the ion fluence increases. This decrease varies from -6.4 % for NWA 4968 to -22.6 % for NWA 7234. Similarly, band depth decreases by -6.4 % for NWA 4968 and -17.5 % for NWA 7234. Note that there is some overlap in the data points associated with our two HEDs, NWA 4968 and NWA 7234, which have similar elemental compositions. All our samples also exhibit reddening across all investigated slopes (Fig. 4 panel c). We detect slope increases varying from  $+0.01~\mu m^{-1}$  for the Band II slope in NWA 6232 to  $+0.30~\mu m^{-1}$  for the Band I slope in NWA 7234. Each dataset from a different pellet seems to follow a different line. Finally, not all of our samples exhibit the same rate of spectral change: for instance, in all three parameter spaces, NWA 4968 and NWA 6909 exhibit a rapid change after the first step of ion implantation and then vary very little after that. On the other hand, NWA 6232 and NWA 7234 do not attain this "effect saturation" even at our highest attained fluence. This effect is especially visible in the Slope space (Fig. 4 panel c).

#### 3.2. Mid-IR data

In mid-IR reflectance, we see changes in the peak position and overall area of the Si—O stretching absorption, around 10 μm (Fig. 5). For NWA 6232, the band area of the feature decreases by approximately 32 % upon ion bombardment, while for NWA 7234, the band area increases by approximately 21 %. A Lorentzian fit over selected spectral intervals is used to derive the positions of the various peaks and shoulders contributing to the shape of the global broad 10-µm feature, along with their associated errors (to compare with the amplitude of the peak position red-shifts for their significance). The selected intervals are highlighted in red in Fig. 5. The peak positions obtained by fitting are shown in Tables 4 and 5 for NWA 6232 and NWA 7234, respectively. We observe a systematic shift towards longer wavelengths, affecting nearly all features. The amplitude of this shift varies from 30 to 170 nm. The most intense features (high in reflectance) sport the most significant spectral shift (coherent with previous experiments in Brunetto et al., 2014). The Christiansen feature (CF) also shifts towards longer wavelengths upon weathering.

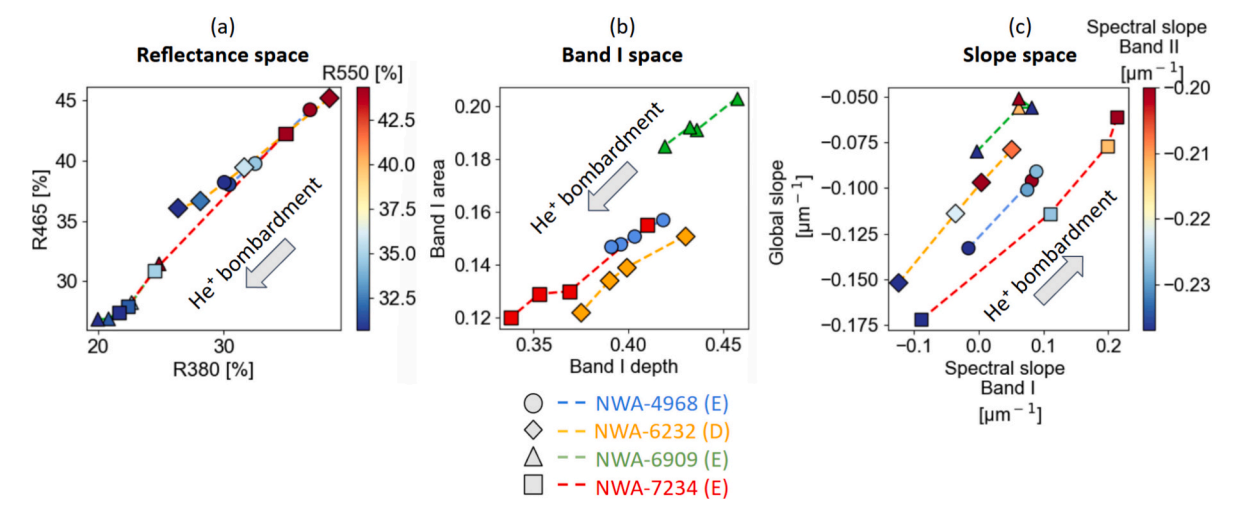


**Fig. 4.** He<sup>+</sup> bombardment induced spectral changes on our HEDs, probed in three parameter spaces. (a) Reflectance space, following the evolution of the reflectance at 380, 465 and 550 nm, with the colorbar being associated with the R550 parameter, highlighting darkening associated with increasing fluence for all the selected reflectances. (b) Band I space, following the evolution of pyroxene Band I depth and area, illustrates the decrease in band area and depth with increasing fluence. (c) Slope space, following the evolution of the global slope, as well as the spectral slopes associated with Band I and Band II, with the colorbar being associated with the Band II slope, highlighting the general reddening of all slopes with the increasing fluence.

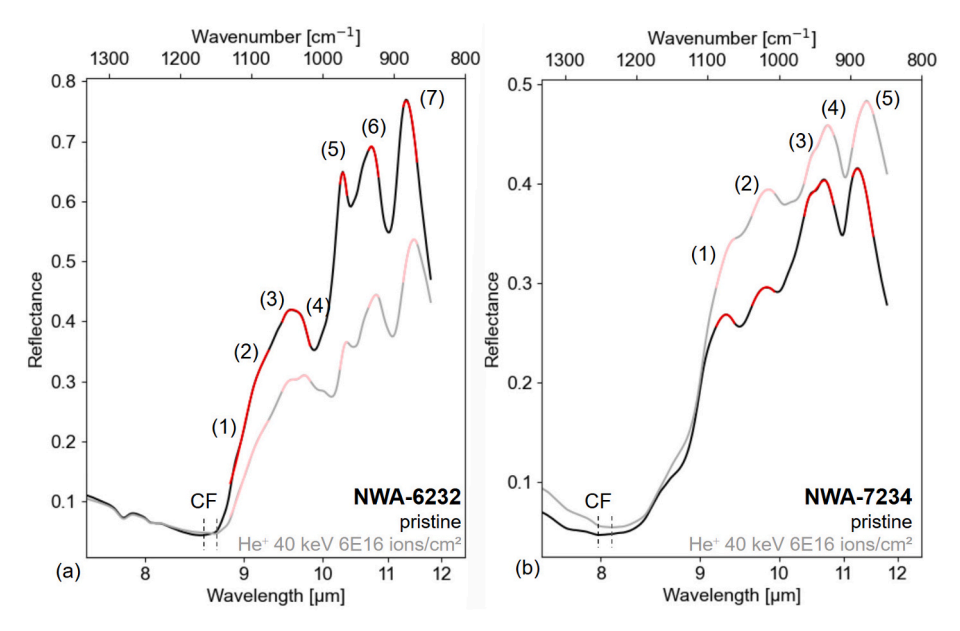


**Fig. 5.** He<sup>+</sup> bombardment induced spectral changes on the NWA 6232 pellet (a) and NWA 7234 pellet (b), probed in the mid-IR. Reflectance spectra associated with pristine (in black) and ion bombarded (in grey) materials. Lorentzian fit intervals, used to identify each peak's position, are in red. (CF: Christiansen feature). The position of the various spectral features (peaks and shoulders) shifts towards longer wavelengths upon ion bombardment. (For interpretation of the references to colour in this figure legend, the reader is referred to the web version of this article.)

Table 4 Peak position changes in NWA 6232 upon 40 keV  ${\rm He}^+$  implantation upon reaching a fluence of 6  $\times$   $10^{16}$  ions/cm². Feature identification based on reference spectra from the USGS library (Kokaly et al., 2017). The LCP signature of the meteorite is a mix of enstatite and ferrosilite, according to the mineralogical composition derived by Carli et al., 2018. (Si-Os: Si—O stretching, CF: Christiansen feature).

|         |                | <u>Fitted position</u><br>Wavenumber in cm <sup>-1</sup><br>Wavelength in µm |                                   |
|---------|----------------|--|-----------------------------------|
| Feature | Identification | Pristine   | 40 keV He <sup>+</sup>            |
| (1)     | Si-Os          | $10949\pm13.2~\text{cm}^{-1}$  | $1101.7 \pm 7 \text{ cm}^{-1}$    |
|         | LCP            | $9.13\pm0.11~\mu m$  | $9.08\pm0.06~\mu m$               |
| (2)     | Si-Os          | $1066.5\pm25.6~{\rm cm}^{-1}$  | $1071.8\pm2.9~{\rm cm}^{-1}$      |
|         | LCP            | $9.38\pm0.22~\mu m$  | $9.33\pm0.02~\mu m$               |
| (3)     | Si-Os          | $1058.8 \pm 0.8~\mathrm{cm^{-1}}$  | $1054.3\pm0.7~{\rm cm^{-1}}$      |
|         | Olivine        | $9.44\pm0.04~\mu m$  | $9.48\pm0.04~\mu m$               |
| (4)     | Si-Os          | $1028.2\pm3.3~{ m cm^{-1}}$  | $1017.8\pm0.8~\rm cm^{-1}$        |
|         | LCP            | $9.72\pm0.13~\mu m$  | $9.82\pm0.02~\mu m$               |
| (5)     | Si-Os          | $971.9 \pm 0.1 \text{ cm}^{-1}$  | $966.7 \pm 0.1 \ cm^{-1}$         |
|         | Olivine        | $10.28\pm0.01~\mu m$   | $10.34\pm0.01~\mu m$              |
| (6)     | Si-Os          | $931.9 \pm 0.1 \ \mathrm{cm^{-1}}$   | $925.1 \pm 0.3~{\rm cm}^{-1}$     |
|         | Olivine        | $10.73\pm0.01~\mu m$   | $10.81\pm0.03~\mu m$              |
| (7)     | Si-Os          | $882.8 \pm 0.2 \ cm^{-1}$  | $872.3 \pm 0.1~\rm cm^{-1}$       |
|         | LCP            | $11.33\pm0.02~\mu\text{m}$   | $11.46\pm0.01~\mu\text{m}$        |
| CF      | -              | $1170.6 \pm 1.4~\mathrm{cm}^{-1}$  | $1151.3 \pm 1.4~\mathrm{cm}^{-1}$ |
|         |                | $8.54\pm0.01~\mu m$  | $8.68\pm0.01~\mu m$               |

#### 4. Discussion

# 4.1. Spectral changes and chemical modifications

We have observed that all samples darken and redden, as well as exhibit a substantial decrease in the Band I feature. The observed behavior is consistent with what has been seen in previous ion bombardment experiments on HEDs (Vernazza et al., 2006; Fulvio et al., 2012; Kanuchova et al., 2015). Darkening and reddening are often associated with creating nanophase Fe particles in anhydrous materials upon weathering (Pieters and Noble, 2016 and references therein). Band I shrinkage may also be related to Fe depletion in the crystal lattice,

Table 5

Peak position changes in NWA 7234 upon 40 keV He+ implantation upon reaching a fluence of  $6\times10^{16}$  ions/cm². Feature identification based on reference spectra from the USGS library (Kokaly et al., 2017). For pyroxene composition, see Carli et al., 2022 (Si-Os: Si—O stretching, Px: pyroxene, Pl: plagioclase, CF: Christiansen feature).

|         |                | $\frac{Fitted\ position}{Wavenumber\ in\ cm^{-1}}$ Wavelength in $\mu m$ |                                   |
|---------|----------------|--|-----------------------------------|
| Feature | Identification | Pristine   | 40 keV He <sup>+</sup>            |
| (1)     | Si-Os          | $1074 \pm 0.1~{\rm cm}^{-1}$   | $1060 \pm 0.2~{\rm cm}^{-1}$      |
|         | Px             | $9.31\pm0.02~\mu m$  | $9.43\pm0.01~\mu m$               |
| (2)     | Si-Os          | $1016.8\pm0.2~{\rm cm^{-1}}$   | $1014.6\pm0.1~{\rm cm}^{-1}$      |
|         | Px or Pl       | $9.83\pm0.01~\mu m$  | $9.86\pm0.01~\mu m$               |
| (3)     | Si-Os          | $964.4 \pm 0.5 \ \mathrm{cm}^{-1}$                                       | $964.5 \pm 0.9 \ cm^{-1}$         |
|         | Px             | $10.36\pm0.01~\mu m$   | $10.36\pm0.02~\mu m$              |
| (4)     | Si-Os          | $930.6 \pm 1.3 \ cm^{-1}$  | $923.9 \pm 0.9~\text{cm}^{-1}$    |
|         | Px or Ol or Pl | $10.74\pm0.02~\mu m$   | $10.82\pm0.01~\mu m$              |
| (5)     | Si-Os          | $890.0 \pm 0.2~\text{cm}^{-1}$   | $877.2 \pm 0.1 \; \rm cm^{-1}$    |
|         | Px or Ol       | $11.23\pm0.01~\mu\text{m}$   | $11.40\pm0.01~\mu m$              |
| CF      | _              | $1251.6 \pm 1.4~\mathrm{cm}^{-1}$  | $1234.2 \pm 1.4~\mathrm{cm}^{-1}$ |
| -       |                | $7.99\pm0.01~\mu m$  | $8.10\pm0.01~\mu m$               |

contributing to the creation of nanophase iron npFe<sup>0</sup> (Brunetto et al., 2014). However, darkening and reddening have also occurred without creating npFe<sup>0</sup> in ion bombarded hydrated minerals, possibly related solely to lattice amorphisation and vesiculation upon ion bombardment (Rubino et al., 2024).

Spectral changes in mid-IR reflectance include variations in the band area of the global Si—O stretching feature and a systematic red shift of its various contributions. It is challenging to comment on band area variations in the mid-IR since the spectra associated with pristine and weathered material originate from different regions of the pellet. Heterogeneities in grain size and differences in grain orientation dominate reflectance levels, complicating the interpretation of band area. On the other hand, these heterogeneities do not affect the position of the absorption features (as seen in Appendix A), indicating that the detected peak position red shift (displacement towards longer wavelengths) of the various absorption features is related to ion bombardment. These

features are not the result of direct vibrational frequencies of chemical bonds but the result of the overlapping of multiple bands, some of which may be masked due to their low intensity (Hamilton, 2000). It is thus delicate to deconvolve the resulting band shape. However, the peak position of these absorption features is still diagnostic of mineral composition and structure. Previous works have detected such red shifts of the Reststrahlen feature in ion bombardment experiments involving ordinary chondrites and carbonaceous chondrites. Preferential sputtering of Mg in the crystal lattice of the ion bombarded material may explain such shifts (Vernazza et al., 2006; Brunetto et al., 2014; Lantz et al., 2017). However, such a shift has also been observed coupled with no elemental changes but only lattice amorphisation (Rubino et al., 2024).

The observed spectral trends in our threefold parameter space suggest that elemental composition is not necessarily the driving factor influencing spectral changes. For instance, the two samples with the closest elemental composition, NWA 4968 and NWA 7234, start their "spectral journey" nearby in both reflectance space and Band I space. However, the rate of their evolution differs right after the first weathering step, with one achieving a degree of weathering maturity close to saturation (NWA 4968) and the other not (NWA 7234). Moreover, these two compositionally similar samples do not "start their journey" nearby in the Slope space. This suggests that another sample property affects the data point distribution more strongly than elemental composition in this space. Even though these two samples are compositionally similar, they differ in regards to mineral variability and grain size distribution, since NWA 4968 consists primarily of a single lithology while NWA 7234 is a brecciated sample.

Similarly, we have observed that two of our samples, NWA 4968 and NWA 6909, exhibit a similar spectral trend (a significant change followed by a more minor change, sometimes even saturation) in almost all parametric spaces. In contrast, the other two samples, NWA 6232 and NWA 7234, do not reach effect saturation even at our highest fluence. This suggests that the property common to each pair of samples is a stronger driver for ion implantation-induced spectral changes than elemental composition. It is relevant to address that the NWA 4968 and NWA 6909 pellets were made with a larger grain size ( $<75\,\mu m$ ) than the NWA 6232 and NWA 7234 pellets ( $<50\,\mu m$ ). The observed dichotomy in behavior further suggests that the grain size difference may affect the weathering rate of ion bombarded samples.

Differences in crystal lattice structure may serve as the driving force, as similar effects have been observed for hydrated serpentines with similar elemental compositions but different lattice configurations upon ion implantation (Rubino et al., 2024). In this case, the different abundances of clinopyroxenes and orthopyroxenes may result in varying amorphization rates across the samples.

Finally, a follow-up study will be dedicated on focused-ion-beam (FIB) sections extracted from these weathered HED pellets, analysed via scanning transmission electron microscopy (STEM), to assess their weathered layers' morphology, potential elemental changes and lattice evolution to better constrain the link between spectral changes and elemental, morphological and lattice modifications on weathered HEDs.

## 4.2. Weathering timescales, saturation and experimental limits

The SIDONIE ion implanter delivered He $^+$  ions with an energy of 40 keV. Although it is ten times higher than the actual energy of the He $^+$  population in the solar wind, we can still derive the corresponding timescale for our highest fluence by estimating the ratio of vacancies per ion of 4 keV He $^+$  to that of 40 keV He $^+$  and by taking into account the contribution of higher energy He $^+$  ions originating by solar flares and active regions. Our highest fluence,  $6 \times 10^{16}$  ions/cm $^2$ , corresponds to  $10^3$ – $10^4$  years of solar wind exposure in the main asteroid belt at 3 AU (see discussion in Brunetto et al., 2014 for more details). Our experiment has highlighted that different samples achieve different degrees of weathering maturity for the same fluence. This implies that different

mineralogical regions of Vesta may reach a state of saturated weathering maturity at different times, depending on their surface properties. However, the timescale for optical alteration by solar-wind ion bombardment is estimated to be 10<sup>4</sup>-10<sup>6</sup> (Vernazza et al., 2006), indicating that, if solar wind ion irradiation were the dominating process at the surface of Vesta, the whole surface should have achieved the same degree of weathering maturity since these are relatively short timescales, especially compared to the age of surfaces and craters on Vesta (10<sup>8</sup> to 10<sup>9</sup> years - O'Brien et al., 2014; Williams et al., 2014). However, there is evidence for a unique kind of SpWe on Vesta (Pieters et al., 2012; McSween Jr et al., 2013), resulting from several effects. For instance, as discussed previously, the presence of a remanent magnetic field originating from the early stage of Vesta as a protoplanet (Fu et al., 2012 and references therein) may partially shield the surface from the effects of solar wind ion irradiation, hence increasing the timescale associated to reach weathering maturity through solar wind ion bombardment. Moreover, surface mixing processes may also contribute in "refreshing" Vesta's surface at different rates: mass wasting associated with gravity driven landslides and slope failures may locally expose great quantities of unweathered surface over shorter timescales (Otto et al., 2013; Krohn et al., 2014a, 2014b), while impact gardening associated with micrometeoroid bombardment causes regolith churning in a more widespread and continuous manner over Vesta's surface and over longer timescales (10<sup>6</sup>–10<sup>8</sup> years, Brunetto et al., 2014), actively working "against" the effects of solar wind ion weathering (Buratti et al., 2013; Denevi et al., 2016). It is relevant to note that, due to its position in the Main Asteroid Belt, impact gardening at Vesta may act at a higher rate than, for instance, our Moon (Housen and Wilkening, 1982), further distancing Vesta's space-weathering regime from the lunar one. Vesta's surface behavior is hence dictated by an ensemble of processes, acting over different timescales in different manners, making the surface appear significantly less weathered than expected (Pieters and Noble, 2016), justifying the search for differences in weathering maturity across Vesta's surface and applying the parameter space presented in this work to the DAWN data.

#### 5. Summary and conclusions

We performed ion bombardment experiments on pressed powder pellets made from four HED meteorites, using 40 keV He ions. This experiment aimed to investigate the effect of space weathering on V-type objects, specifically the impact of the solar wind component of space weathering. Spectral changes induced by weathering include significant darkening and reddening in the visible range, accompanied by the shrinkage of Band I and the red shift of the peak position of the Si—O stretching features in the mid-IR. The parameter space described in this work indicates that elemental composition is not the primary factor driving spectroscopic evolution upon weathering for HEDs. A follow-up study will investigate a smaller scale using electron microscopy to assess morphological and elemental changes at the surface of ion-bombarded pellets, while another will apply the parameter space described in this work to Vesta remote-sensed data.

## CRediT authorship contribution statement

Stefano Rubino: Writing – review & editing, Writing – original draft, Visualization, Validation, Methodology, Investigation, Formal analysis, Data curation, Conceptualization. Francesca Zambon: Writing – review & editing, Visualization, Validation, Supervision, Resources, Project administration, Methodology, Funding acquisition, Formal analysis, Conceptualization. Rosario Brunetto: Writing – review & editing, Visualization, Validation, Supervision, Resources, Methodology, Investigation, Data curation. Océane Barraud: Writing – review & editing. Sébastien Besse: Writing – review & editing. Ferenc Borondics: Writing – review & editing. Cristian Carli: Writing – review & editing, Validation, Investigation. Jean-Philippe Combe: Writing –

review & editing. Kerri Donaldson-Hanna: Writing – review & editing. Rachel Klima: Writing – review & editing. Cateline Lantz: Writing – review & editing, Investigation, Data curation. Giovanni Pratesi: Writing – review & editing, Resources. Katrin Stephan: Writing – review & editing. Federico Tosi: Writing – review & editing, Validation, Resources, Methodology, Investigation.

#### Declaration of competing interest

None.

#### Acknowledgements

We thank O. Mivumbi, J. Boderfois and P. Benoit-Lamaitrie for help

and technical support with SIDONIE and INGMAR. INGMAR is a joint IAS-IJCLab (Orsay, France) facility funded by the P2IO LabEx (ANR-10-LABX-0038) in the framework Investissements d'Avenir (ANR-11-IDEX-0003-01). The authors wish to thank the editor as well as the two anonymous reviewers for their precious insight. SR is supported by the ASI-INAF agreement n.2023-6-HH.0. This research was supported by the International Space Science Institute (ISSI) in Bern through ISSI International Team project n°485 (Deciphering Compositional Processes in Inner Airless Bodies of our Solar System). The data that support the findings of this study are available from the corresponding author, SR, upon reasonable request.

#### Appendix A. Mid-IR spectra and pellet homogeneity

Hyperspectral maps over ROIs of  $704 \times 704$  µm, with a spatial resolution of 5.5 µm, were acquired at the center of the pellets as well as over the threshold between the bombarded and the non-bombarded regions over the pellet rim, using a Focal Plane Array (FPA) detector. The center of the pellets could not be characterized before the weathering experiment due to experimental scheduling constraints. Hence, in the mid-IR, the pristine and the ion bombarded spectra come from different pellet regions. This may complicate the data interpretation. However, the hyperspectral maps allowed us to estimate that these pressed-powder pellets are mineralogically homogeneous enough for such a comparison at the scale of the maps (spectra are associated with ROIs at least larger than  $200 \times 200$  µm). In Figs. A1 and A2, we compare the ion bombarded spectra obtained from the center of the pellets to the one derived from ROIs located next to the threshold between ion bombarded and pristine material at the pellets' rim. The observed spectral differences are due to different crystal orientations, not mineral distribution since the spectral peak position does not change between the ROIs.

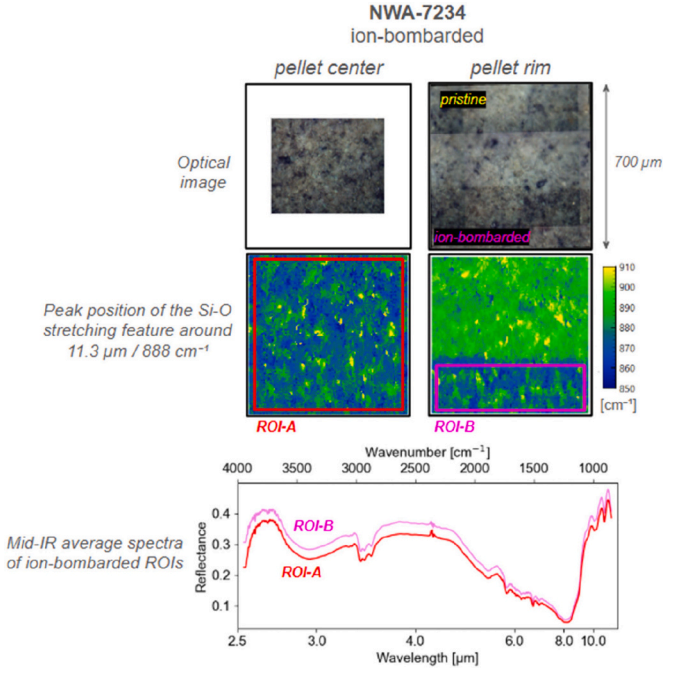


Fig. A1. Mineral homogeneity of pellet NWA 6232: ROIs and associated average spectra of ion bombarded material from the center and the pellet's rim.

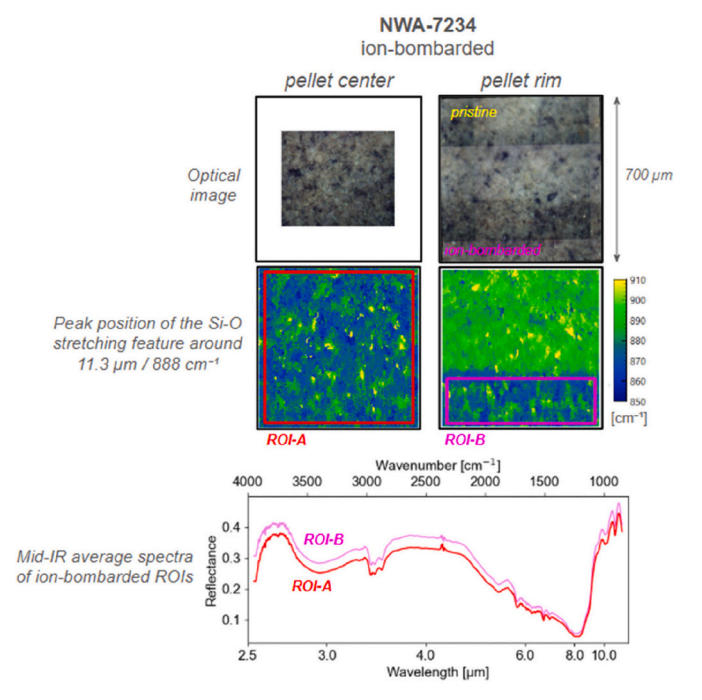
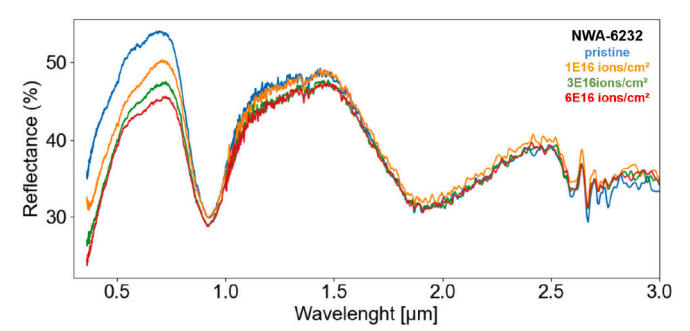


Fig. A2. Mineral homogeneity of pellet NWA 7234: ROIs and associated average spectra of ion bombarded material from the center and the pellet's rim.

# Appendix B. Complete visible to near-IR dataset

This appendix section presents the complete visible to near-IR spectral dataset of our He<sup>+</sup> ion bombarded HEDs. The dataset for NWA 4968, already shown in Fig. 3.1, is not repeated here.



**Fig. B1.** Spectral dataset of the NWA 6232 pellet, wavelength vs. reflectance. Evolution of NWA 6232 upon 40 keV He<sup>+</sup> ion implantation from 0.3 to 3 μm. Fluences from top to bottom near 700 nm: 0 ions/cm<sup>2</sup> (pristine),  $1 \times 10^{16}$  ions/cm<sup>2</sup>,  $3 \times 10^{16}$  ions/cm<sup>2</sup>,  $6 \times 10^{16}$  ions/cm<sup>2</sup>.

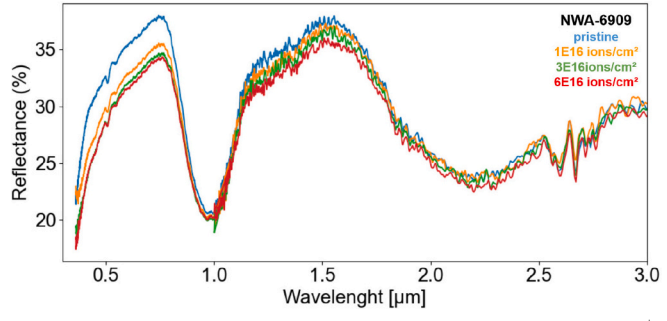


**Fig. B2.** Spectral dataset of the NWA 6909 pellet, wavelength vs. reflectance. Evolution of NWA 6909 upon 40 keV He<sup>+</sup> ion implantation from 0.3 to 3 μm. Fluences from top to bottom near 700 nm: 0 ions/cm<sup>2</sup> (pristine),  $1 \times 10^{16}$  ions/cm<sup>2</sup>,  $3 \times 10^{16}$  ions/cm<sup>2</sup>,  $6 \times 10^{16}$  ions/cm<sup>2</sup>.

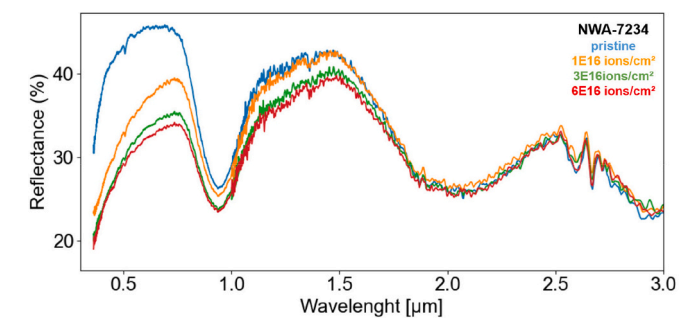


Fig. B3. Spectral dataset of the NWA 7234 pellet, wavelength vs. reflectance. Evolution of NWA 7234 upon 40 keV He $^+$  ion implantation from 0.3 to 3  $\mu$ m. Fluences from top to bottom near 700 nm: 0 ions/cm $^2$  (pristine),  $1 \times 10^{16}$  ions/cm $^2$ ,  $3 \times 10^{16}$  ions/cm $^2$ ,  $6 \times 10^{16}$  ions/cm $^2$ .

# Appendix C. Evolution of all considered parameters

The following Figure showcases the individual evolution of the 25 parameters discussed in the initial part of the Results section. The  $\rho$  index quantifies the parameter's variability, as presented in section III.1, formula (1).

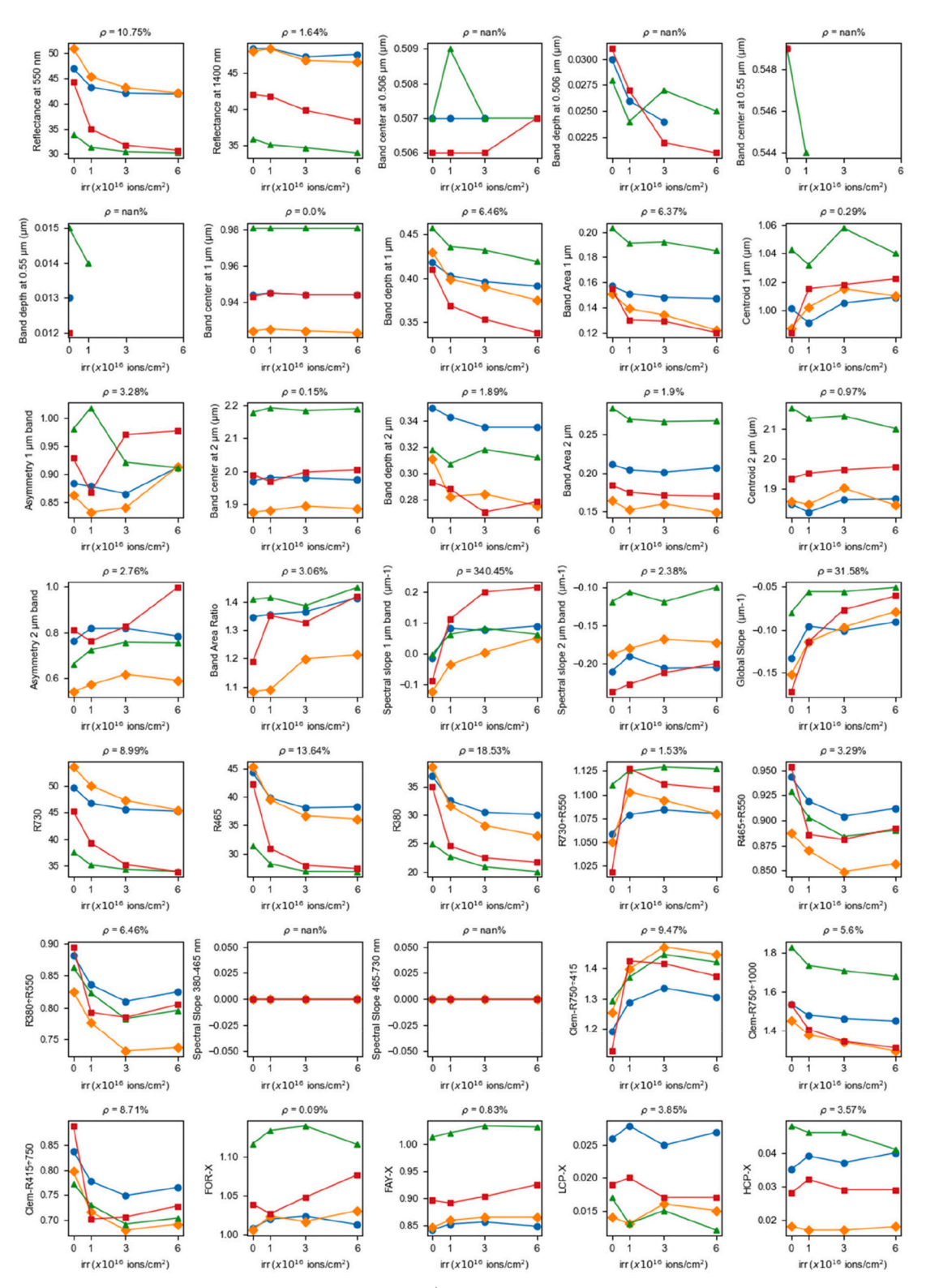


Fig. C1. Evolution of all 25 individual spectral parameters as a function of He<sup>+</sup> ion fluence. The figure legend is as follows: NWA 4968 in blue, circular marker; NWA 6232 in orange, diamond-shaped marker; NWA 6909 in green, triangle marker; NWA 7234 in red, square marker. (For interpretation of the references to colour in this figure legend, the reader is referred to the web version of this article.)

# Data availability

Data will be made available in the SSHADE/Daisy repository once the paper is accepted.

#### References

Ammannito, E., De Sanctis, M.C., Palomba, E., Longobardo, A., Mittlefehldt, D.W., McSween, H.Y., Marchi, S., et al., 2013. Olivine in an unexpected location on Vesta's surface. Nature 504 (7478), 122–125.

- Binzel, Richard P., Gaffey, Michael J., Thomas, Peter C., Zellner, Benjamin H., Storrs, Alex D., Wells, Eddie N., 1997. Geologic mapping of Vesta from 1994 Hubble space telescope images. Icarus 128 (1), 95–103.
- Brunetto, R., Strazzulla, G., 2005. Elastic collisions in ion irradiation experiments: a mechanism for space weathering of silicates. Icarus 179 (1), 265–273.
- Brunetto, R., Lantz, C., Ledu, D., Baklouti, D., Barucci, M.A., Beck, P., Delauche, L., et al., 2014. Ion irradiation of Allende meteorite probed by visible, IR, and Raman spectroscopies. Icarus. https://doi.org/10.1016/j.icarus.2014.04.047.
- Brunetto, R., Lantz, C., Nakamura, T., Baklouti, D., Le Pivert-Jolivet, T., Kobayashi, S., Borondics, F., 2020. Characterizing irradiated surfaces using IR spectroscopy. Icarus 345 (113722), 113722.
- Buratti, B.J., Dalba, P.A., Hicks, M.D., Reddy, V., Sykes, M.V., McCord, T.B., O'Brien, D. P., et al., 2013. Vesta, Vestoids, and THE HED meteorites: interconnections and differences based onDawnFraming camera observations: vesta, vestoids, and the hed meteorites. J. Geophys. Res. Planets 118 (10), 1991–2003.
- Carli, Cristian, Pratesi, Giovanni, Moggi-Cecchi, Vanni, Zambon, Francesca, Capaccioni, Fabrizio, Santoro, Simone, 2018. Northwest Africa 6232: visible-near infrared reflectance spectra variability of an olivine Diogenite. Meteorit. Planet. Sci. 53 (10), 2228–2242.
- Carli, Cristian, Ciarniello, Mauro, Migliorini, Alessandra, Pratesi, Giovanni, 2022. Iron rich basaltic Eucrites, implication on spectral properties and parental bodies. Icarus 371 (January), 114653.
- Chauvin, N., Dayras, F., Le Du, D., Meunier, R., 2004. SIDONIE: an electromagnetic isotope separator for preparation of high purity thin targets. Nucl. Instrum. Methods Phys. Res., Sect. A 521 (1), 149–155.
- Clark, Roger N., Roush, Ted L., 1984. Reflectance spectroscopy: quantitative analysis techniques for remote sensing applications. J. Geophys. Res. 89 (B7), 6329–6340.
- Cloutis, Edward A., Klima, Rachel L., Lindsay Kaletzke, A., Coradini, L.F., Golubeva, L.A., McFadden, D.I., Shestopalov, and F. Vilas., 2010. The 506nm absorption feature in pyroxene spectra: nature and implications for spectroscopy-based studies of pyroxene-bearing targets. Icarus 207 (1), 295–313.
- Cloutis, E.A., Gaffey, M.J., 1991. Pyroxene spectroscopy revisited: Spectral-compositional correlations and relationship to geothermometry. J. Geophys. Res. 96 (E5), 22809–22826. https://doi.org/10.1029/91JE02512.
- Combe, Jean-Philippe, McCord, Thomas B., McFadden, Lucy A., Ieva, Simone, Tosi, Federico, Longobardo, Andrea, Frigeri, Alessandro, et al., 2015. Composition of the northern regions of Vesta analyzed by the Dawn Mission. Icarus 259 (October), 53–71.
- Cuzzi, Jeff, Clark, Roger, Filacchione, Gianrico, French, Richard, Johnson, Robert, Marouf, Essam, Spilker, Linda, 2009. Ring particle composition and size distribution. In: Saturn from Cassini-Huygens. Springer Netherlands, Dordrecht, pp. 459–509.
- De Sanctis, M.C., Ammannito, E., Capria, M.T., Tosi, F., Capaccioni, F., Zambon, F., Carraro, F., et al., 2012. Spectroscopic characterization of mineralogy and its diversity across Vesta. Science 336 (6082), 697–700.
- De Sanctis, M., Cristina, Eleonora Ammannito, Teresa Capria, M., Capaccioni, Fabrizio, Combe, Jean-Philippe, Frigeri, Alessandro, Longobardo, Andrea, et al., 2013. Vesta's mineralogical composition as revealed by the visible and infrared spectrometer on Dawn. Meteorit. Planet. Sci. 48 (11), 2166–2184.
- Denevi, B.W., Lucey, P.G., Hochberg, E.J., Steutel, D., 2007. Near-infrared optical constants of pyroxene as a function of Iron and calcium content. J. Geophys. Res. 112 (E5). https://doi.org/10.1029/2006je002802.
- Denevi, Brett W., Beck, Andrew W., Coman, Ecaterina I., Thomson, Bradley J., Ammannito, Eleonora, Blewett, David T., Sunshine, Jessica M., et al., 2016. Global variations in regolith properties on asteroid Vesta from Dawn's low-altitude mapping orbit. Meteorit. Planet. Sci. 51 (12), 2366–2386.
- Denevi, Brett W., Noble, Sarah K., Christoffersen, Roy, Thompson, Michelle S., Glotch, Timothy D., Blewett, David T., Garrick-Bethell, Ian, et al., 2024. 14 space weathering at the moon. In: New View of the Moon, vol. 2. De Gruyter, pp. 611–650.
- Donaldson Hanna, K.L., Thomas, I.R., Bowles, N.E., Greenhagen, B.T., Pieters, C.M., Mustard, J.F., Jackson, C.R.M., Wyatt, M.B., 2012. Laboratory emissivity measurements of the plagioclase solid solution series under varying environmental conditions. J. Geophys. Res. 117, E11004. https://doi.org/10.1029/2012.JE004184
- conditions. J. Geophys. Res. 117, E11004. https://doi.org/10.1029/2012JE004184. Filacchione, G., Capaccioni, F., Ciarniello, M., Clark, R.N., Cuzzi, J.N., Nicholson, P.D., Cruikshank, D.P., et al., 2012. Saturn's icy satellites and rings investigated by Cassini–VIMS: III radial compositional variability. Icarus 220 (2), 1064–1096.
- Fu, Roger R., Weiss, Benjamin P., Shuster, David L., Gattacceca, Jérôme, Grove, Timothy L., Suavet, Clément, Lima, Eduardo A., Li, Luyao, Kuan, Aaron T., 2012. An Ancient Core Dynamo in Asteroid Vesta. Science (New York, N.Y.) 338 (6104), 238–241.
- Fulvio, D., Brunetto, R., Vernazza, P., Strazzulla, G., 2012. Space weathering of Vesta and V-type asteroids: new irradiation experiments on HED meteorites. Astron. Astrophys., Suppl. Ser. 537 (January), L11.
- Hamilton, Victoria E., 2000. Thermal infrared emission spectroscopy of the pyroxene mineral series. J. Geophys. Res. 105 (E4), 9701–9716.
- Hiroi, T., Pieters, C.M., 1998. Origin of Vestoids suggested from the space weathering trend in the visible reflectance spectra of HED meteorites and lunar soils. Antarct. Meteorite Res. 11, 163–170. https://adsabs.harvard.edu/full/seri/AMR../00 11/0000170.000.html.
- Hiroi, Takahiro, Pieters, Carlé M., Takeda, Hiroshi, 1994. Grain size of the surface regolith of asteroid 4 Vesta estimated from its reflectance Spectrum in comparison with HED meteorites. Meteoritics 29 (3), 394–396.
- Hiroi, T., Sasaki, S., Misu, T., Nakamura, T., 2013. Keys to Detect Space Weathering on Vesta: Changes of Visible and Near-Infrared Reflectance Spectra of HEDs and Carbonaceous Chondrites, p. 1276.
- Housen, K.R., Wilkening, L.L., 1982. Regoliths on small bodies in the solar system. Annu. Rev. Earth Planet. Sci. 10 (1), 355–376.

Jaumann, R., Williams, D.A., Buczkowski, D.L., Yingst, R.A., Preusker, F., Hiesinger, H., Schmedemann, N., et al., 2012. Vesta's Shape and Morphology. Science (New York, N.Y.) 336 (6082), 687–690.

- Kanuchova, Z., Brunetto, R., Fulvio, D., Strazzulla, G., 2015. Near-ultraviolet bluing after space weathering of silicates and meteorites. Icarus 258 (September), 289–296.
- Klima, Rachel L., Pieters, Carlé M., Darby Dyar, M., 2007. Spectroscopy of synthetic Mg-Fe pyroxenes I: spin-allowed and spin-forbidden crystal field bands in the visible and near-infrared. Meteorit. Planet. Sci. 42 (2), 235–253.
- Kokaly, Raymond F., Clark, Roger N., Swayze, Gregg A., Eric Livo, K., Hoefen, Todd M., Pearson, Neil C., Wise, Richard A., et al., 2017. USGS Spectral Library Version 7. US Geological Survey, Data Series. https://doi.org/10.3133/ds1035.
- Krohn, K., Jaumann, R., Elbeshausen, D., Kneissl, T., Schmedemann, N., Wagner, R., Voigt, J., et al., 2014a. Asymmetric craters on Vesta: impact on sloping surfaces. Planet. Space Sci. 103 (November), 36–56.
- Krohn, K., Jaumann, R., Otto, K., Hoogenboom, T., Wagner, R., Buczkowski, D.L., Garry, B., et al., 2014b. Mass movement on Vesta at steep scarps and crater rims. Icarus 244 (December), 120–132.
- Lantz, C., Brunetto, R., Barucci, M.A., Dartois, E., Duprat, J., Engrand, C., Godard, M., Ledu, D., Quirico, E., 2015. Ion irradiation of the Murchison meteorite: visible to mid-infrared spectroscopic results. Astron. Astrophys. https://doi.org/10.1051/ 0004-6361/201425398.
- Lantz, C., Brunetto, R., Barucci, M.A., Fornasier, S., Baklouti, D., Bourçois, J., Godard, M., 2017. Ion irradiation of carbonaceous chondrites: a new view of space weathering on primitive asteroids. Icarus 285 (March), 43–57.
- Li, Jian-Yang, Bodewits, Dennis, Feaga, Lori M., Landsman, Wayne, A'Hearn, Michael F., Mutchler, Max J., Russell, Christopher T., McFadden, Lucy A., Raymond, Carol A., 2011. Ultraviolet spectroscopy of asteroid (4) Vesta. Icarus 216 (2), 640–649.
- McCord, T.B., Adams, J.B., Johnson, T.V., 1970. Asteroid Vesta: spectral reflectivity and compositional implications. Science 168 (3938), 1445–1447.
- McCord, T.B., Li, J.-Y., Combe, J.-P., McSween, H.Y., Jaumann, R., Reddy, V., Tosi, F., et al., 2012. Dark material on Vesta from the Infall of carbonaceous volatile-rich material. Nature 491 (7422), 83–86.
- McSween Jr., Harry Y., Binzel, Richard P., Cristina De Sanctis, M., Ammannito, Eleonora, Prettyman, Thomas H., Beck, Andrew W., Reddy, Vishnu, et al., 2013. Dawn; the Vesta–HED connection; and the geologic context for Eucrites, Diogenites, and Howardites. Meteorit. Planet. Sci. 48 (11), 2090–2104.
- Mittlefehldt, David W., 2015. Asteroid (4) Vesta: I. The Howardite-Eucrite-Diogenite (HED) clan of meteorites. Chem. Erde 75 (2), 155–183.
- Mittlefehldt, David W., Greenwood, Richard C., Berger, Eve L., Le, Loan, Peng, Zhan X., Kent Ross, D., Goodrich, Cyrena, 2022. Eucrite-type Achondrites: petrology and oxygen isotope compositions. Meteorit. Planet. Sci. 57 (2), 484–526.
- Noble, S.K., Keller, L.P., Pieters, C.M., 2010a. Evidence of space weathering in regolith breccias II: Asteroidal regolith breccias. Meteorit. Planet. Sci. 45, 2007–2015. https://doi.org/10.1111/j.1945-5100.2010.01151.x.
- Noble, S.K., Keller, L.P., Pieters, C.M., 2010b. Evidence of space weathering in regolith breccias II: Asteroidal regolith breccias. Meteorit. Planet. Sci. 45, 2007–2015. https://doi.org/10.1111/j.1945-5100.2010.01151.x.
- Noguchi, Takaaki, Kimura, Makoto, Hashimoto, Takahito, Konno, Mitsuru, Nakamura, Tomoki, Zolensky, Michael E., Okazaki, Ryuji, et al., 2014. Space weathered rims found on the surfaces of the Itokawa dust particles. Meteorit. Planet. Sci. 49 (2), 188–214.
- O'Brien, D., Marchi, S., Morbidelli, A., Bottke, W., Schenk, P., Russell, C., Raymond, C., 2014. The impact history of Vesta. Vesta in the Light of Dawn: First Exploration of a Protoplanet in the Asteroid Belt 1773 (February), 2049.
- Ohtake, Makiko, Matsunaga, Tsuneo, Haruyama, Junichi, Yokota, Yasuhiro, Morota, Tomokatsu, Honda, Chikatoshi, Ogawa, Yoshiko, et al., 2009. The global distribution of pure Anorthosite on the moon. Nature 461 (7261), 236–240.
- Otto, Katharina A., Jaumann, Ralf, Krohn, Katrin, Matz, Klaus-Dieter, Preusker, Frank, Roatsch, Thomas, Schenk, Paul, et al., 2013. Mass-wasting features and processes in Vesta's south Polar Basin RHEASILVIA: RHEASILVIA MASS WASTING. J. Geophys. Res. Planets 118 (11), 2279–2294.
- Park, R.S., Ermakov, A.I., Konopliv, A.S., Vaughan, A.T., Rambaux, N., Bills, B.G., Castillo-Rogez, J.C., et al., 2025. A small Core in Vesta inferred from Dawn's observations. Nature Astron. https://doi.org/10.1038/s41550-025-02533-7. April.
- Pieters, Carle M., Noble, Sarah K., 2016. Space weathering on airless bodies. J. Geophys. Res. Planets 121 (10), 1865–1884.
- Pieters, C.M., Ammannito, E., Blewett, D.T., Denevi, B.W., De Sanctis, M.C., Gaffey, M.J., Le Corre, L., et al., 2012. Distinctive space weathering on Vesta from regolith mixing processes. Nature 491 (7422), 79–82.
- Poulet, F., Ruesch, O., Langevin, Y., Hiesinger, H., 2015. Modal mineralogy of the surface of Vesta: evidence for ubiquitous olivine and identification of meteorite analogue. Icarus 253 (June), 364–377.
- Reddy, Vishnu, Le Corre, Lucille, O'Brien, David P., Nathues, Andreas, Cloutis, Edward A., Durda, Daniel D., Bottke, William F., et al., 2012. Delivery of dark material to Vesta via carbonaceous chondritic impacts. Icarus 221 (2), 544–559.
- Rubino, S., Lantz, C., Baklouti, D., Leroux, H., 2020. Space weathering affects the remote near-IR identification of phyllosilicates. The Planet. Sci. J. 1, 61. https://iopscience. iop.org/article/10.3847/PSJ/abb94c/pdf.
- Rubino, Stefano, Potin, Sandra, Lantz, Cateline, Baklouti, Donia, Beck, Pierre, Brissaud, Olivier, Leroux, Hugues, et al., 2022. Geometry induced Bias in the remote near-IR identification of phyllosilicates on space weathered bodies. Icarus 376 (April), 114887.
- Rubino, Stefano, Leroux, Hugues, Lantz, Cateline, Aléon-Toppani, Alice, Baklouti, Donia, Djouadi, Zahia, Mivumbi, Obadias, Troadec, David, Borondics, Ferenc, Brunetto, Rosario, 2024. Space-weathering induced changes in hydrated silicates: a

- multi-scale study combining visible/infrared spectroscopy and Electron microscopy. Icarus 415 (116070), 116070.
- Russell, Christopher, Raymond, Carol, 2012. The Dawn Mission to Minor Planets 4 Vesta and 1 Ceres. Springer Science & Business Media.
- Scott, Edward R.D., Greenwood, Richard C., Franchi, Ian A., Sanders, Ian S., 2009.
  Oxygen isotopic constraints on the origin and parent bodies of Eucrites, Diogenites, and Howardites. Geochim. Cosmochim. Acta 73 (19), 5835–5853.
- Speyerer, Emerson J., Robinson, Mark S., Boyd, Aaron, Silva, Victor H., Lawrence, Samuel, 2023. Precise mapping of the moon with the Clementine ultraviolet/visible camera. Icarus 398 (115506), 115506.
- Toplak, Marko, Read, Stuart T., Sandt, Christophe, Borondics, Ferenc, 2021. Quasar: easy machine learning for biospectroscopy. Cells (Basel, Switzerland) 10 (9), 2300.
- Vernazza, P., Brunetto, R., Strazzulla, G., Fulchignoni, M., Rochette, P., Meyer-Vernet, N., Zouganelis, I., 2006. Asteroid colors: a novel tool for magnetic field detection? The case of Vesta. Astron. Astrophys. 451 (3), L43–L46.
- Williams, D.A., Jaumann, R., McSween, H.Y., Marchi, S., Schmedemann, N., Raymond, C. A., Russell, C.T., 2014. The Chronostratigraphy of Protoplanet Vesta. Icarus 244 (December), 158–165.
- Zambon, F., Brunetto, R., Combe, J., Klima, Rachel L., Rubino, Stefano, Katrin Stephan, F., Tosi, et al., 2022. New updates from ISSI project N° 485, deciphering compositional processes in inner airless bodies of our solar system. Asteroids, Comets, Meteors Conference 2851, 2394.
- Ziegler, James F., Ziegler, M.D., Biersack, J.P., 2010. SRIM the stopping and range of ions in matter (2010). Nucl. Instrum. Methods Phys. Res., Sect. B 268 (11–12), 1818–1823.